Ultra-high resolution steady-state micro-thermometry using a bipolar direct current reversal technique

Jason Yingzhi Wu, Wei Wu, and Michael Thompson Pettes[a)]
Department of Mechanical Engineering and Institute of Materials Science, University of Connecticut, Storrs, Connecticut 06269, USA

The suspended micro-thermometry measurement technique is one of the most prominent methods for probing the in-plane thermal conductance of low dimensional materials, where a suspended microdevice containing two built-in platinum resistors that serve as both heater and thermometer is used to measure the temperature and heat flow across a sample. The presence of temperature fluctuations in the sample chamber and background thermal conductance through the device, residual gases, and radiation are dominant sources of error when the sample thermal conductance is comparable to or smaller than the background thermal conductance, on the order of 300 pW/K at room temperature. In this work, we present a high resolution thermal conductance measurement scheme in which a bipolar direct current reversal technique is adopted to replace the lock-in technique. We have demonstrated temperature resolution of 1.0–2.6 mK and thermal conductance resolution of 1.7–26 pW/K over a temperature range of 30–375 K. The background thermal conductance of the suspended microdevice is determined accurately by our method and allows for straightforward isolation of this parasitic signal. This simple and high-throughput measurement technique yields an order of magnitude improvement in resolution over similarly configured lock-in amplifier techniques, allowing for more accurate investigation of fundamental phonon transport mechanisms in individual nanomaterials. *Published by AIP Publishing.* [http://dx.doi.org/10.1063/1.4962714]

I. INTRODUCTION

Low dimensional materials such as carbon nanotubes,[1–6] inorganic nanowires,[7–12] organic nanofibers,[13–15] superlattices,[16,17] and two dimensional materials[18–24] have been the focus of significant research interest over the past two decades due to their unique thermal transport properties which can be significantly different than those in their bulk form. In addition to establishing fundamental structure-property relationships in these materials, these investigations have also enabled novel thermal device applications.[25–29] Hence, further development of new experimental techniques for characterization of thermal transport in nanostructures remains an important area as advancement continues in the prediction, design, and synthesis of new materials.

Several thermal measurement techniques have been developed for probing in-plane thermal transport properties in low dimensional materials, the most prominent of which are the suspended micro-thermometry,[1,2,4,11,19,30] Raman thermometry,[5,18,31] bi-material atomic force microscopy cantilever,[13] and steady-state Joule heating[4,32–34] methods. Of these, the suspended micro-thermometry technique is the most common method to measure in-plane thermal conductance in individual nanostructures as phonons are fully thermalized, in contrast to optothermal techniques.[35,36] Platinum resistance thermometers (PRTs) are used to measure the temperature and heat flow on the suspended microdevice as platinum's electrical resistivity has a nearly linear relationship with temperature in addition to a large temperature coefficient of resistance (TCR) over a wide range of temperatures. Based upon the original reports,[1,2] several different electrical resistance measurement techniques have been developed to achieve higher temperature and thermal conductance resolution in the suspended micro-thermometry method.[37–39] A summary of these techniques is shown in Table I.

In previous lock-in amplifier-based measurement schemes,[1,2] the thermal conductance resolution is on the order of 1 nW/K. Previous improvements on the micro-thermometry technique have resulted in two major contributions. First, the voltage noise and ambient temperature drift that arise from an unmodulated temperature signal can be eliminated using a high frequency detection current with a lock-in amplifier and a differential scheme,[37,38] but a complicated setup and data analysis is involved to achieve this high temperature and thermal conductance resolution. Second, when the temperature on the sensing membrane is modulated at specific frequency, an unmodulated sensing current can be used to further improve temperature resolution;[39,40] however, the attenuation of modulated temperature due to the large thermal time constants of suspended microdevices becomes an issue during the thermal conductance measurement.

In this work, we have developed a simple suspended micro-thermometry measurement scheme involving less instrumentation and straightforward data analysis. Specifically, we have introduced a bipolar DC reversal method which is a well-established alternative technique to remove offset and low frequency noises during measurement. This technique exhibits less than one half the amount of white noise and an order of magnitude lower $1/f$ noise than the most commonly

---

[a)]Author to whom correspondence should be addressed. Electronic mail: michael.pettes@uconn.edu

87, 094901-1

TABLE I. Summary of micro-resistance thermometry-based techniques. Noise equivalent temperature resolution of the sensing thermometer (NET$_s$) and noise equivalent thermal conductance resolution (NEG) are the critical performance parameters in these methods.

Temperature measurement scheme[a]	Heating current[b]	Sensing current[c]	NET$_s$[d]	NEG[d]	Comment
Lock-in[2]	Unmodulated	Modulated	25 mK (300 K)	1 nW/K (300 K)	One of the first suspended micro-thermometry techniques to measure the in-plane thermal conductance of an individual nanostructure. Background thermal conductance becomes an issue when G_s is comparable to G_{bg}, on the order of 200–400 pW/K.
Lock-in, differential[38]	Unmodulated	Modulated	10 mK (320 K)	100 pW/K (320 K)	Eliminates error contributed from background thermal conductance, parasitic heat loss from the supporting beams, and device asymmetry. However, the method involves laborious data analysis and multiple measurement schemes.
Lock-in, differential[40]	Modulated	Unmodulated	20 μK (280 K)	N/A	Resistance-based high-resolution thermometer, which improves signal-to-noise ratio through higher common mode noise rejection. The differential technique eliminates the error arising from ambient temperature fluctuation, on the order of 5 mK.
Lock-in, Wheatstone bridge[39]	Modulated	Unmodulated	50 μK (300 K)	0.25 pW/K (300 K)	Modification of the suspended micro-thermometry technique which improves signal-to-noise ratio using a Wheatstone bridge circuit to amplify the AC signal while eliminating the error arising from the ambient temperature fluctuation.
DC reversal (this work)	Unmodulated	Modulated	1.6 mK (290 K)	13 pW/K (290 K)	Modification of the suspended micro-thermometry technique which improves signal-to-noise ratio through a measurement scheme benefitting from improved common mode noise rejection over lock-in amplifier-based techniques (200 dB versus 100 dB). High throughput, simple measurement scheme, and fewer sources of error and noise.

[a]Differential indicates adoption of a matching resistance to cancel ambient temperature fluctuations. Wheatstone bridge indicates adoption of a Wheatstone bridge circuit to cancel ambient temperature fluctuations.
[b]Unmodulated indicates a steady-state temperature rise induced by a DC current, and modulated indicates an oscillating temperature rise with a frequency $2f$ induced by an AC current at f.
[c]Unmodulated indicates detection of resistance by applying a DC current, and modulated indicates detection using an AC current with a frequency f.
[d]Corresponding ambient temperatures for reported NET$_s$ and NEG values are given in parentheses.

used lock-in amplifiers.[41] As a result, we have demonstrated resolution near the instrumentation limit of this technique: a sensing noise equivalent temperature (NET$_s$) of 2.62 and 1.12 mK and a noise equivalent thermal conductance (NEG) of 26.42 and 1.73 pW/K at an ambient temperature of 375 and 30 K, respectively. The NET$_s$ reaches a minimum of 0.83 mK at 100 K without the need for using complicated schemes involving matching resistors or a Wheatstone bridge to cancel the ambient temperature drift.

II. MEASUREMENT SETUP

A schematic of the measurement is shown in Figure 1. The suspended microdevice contains two symmetric adjacent silicon nitride (SiN$_x$, 22 μm by 22 μm) membranes, each suspended by six 400 μm long SiN$_x$ beams. A serpentine PRT is fabricated on each membrane and connects to four contact pads by platinum lines on the suspended beams. The silicon substrate beneath the suspended membranes is completely removed. Details of the fabrication process are given in Ref. 42. The suspended microdevice was placed in a Janis SHI-4ST-UHV closed cycle cryostat connected to an Oerlikon Leybold TURBOVAC TW250S/TRIVAC D16BCS turbo pumping system providing a vacuum environment better than 10^{-8} mbar during thermal transport measurements. The cryostat ambient temperature was controlled by a Lakeshore 336 cryogenic temperature controller. On one suspended membrane denoted as the heating membrane, the PRT was electrically heated by an unmodulated current provided by a Keithley 6517B electrometer in series with a 10 MΩ high precision resistor (Caddock USF370-10.0M-0.01%-5 ppm). The DC current passing through the device was directly measured by the low-impedance input of the Keithley 6517B. During the measurement, a certain amount of this heat
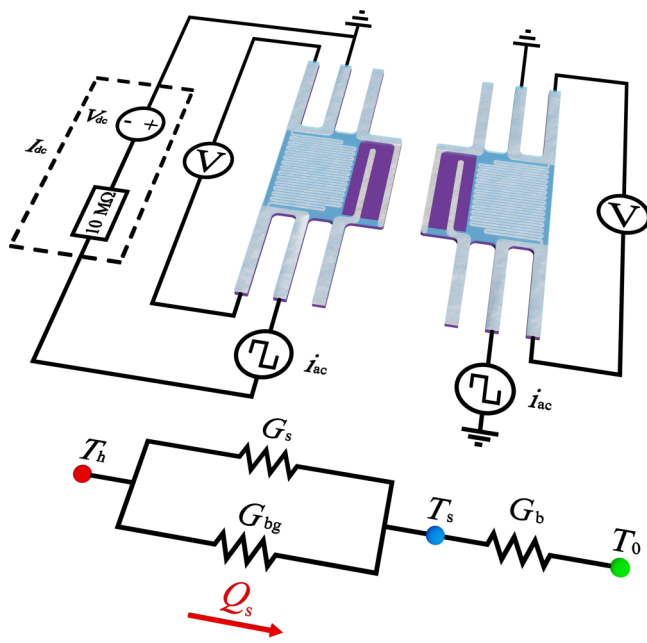
FIG. 1. Circuit diagram of the DC reversal technique developed to measure the electrical resistances of the heating and sensing PRTs of a suspended microdevice. Shown below is the corresponding thermal circuit. A 10 MΩ ultra high precision resistor is used to convert the voltage source (Keithley 6517B) into the DC heating current to the heating PRT, I_{dc}. A high input impedance programmable current source (10^{14} Ω, Keithley 6221) and high input impedance nanovoltmeter ($>10^{12}$ Ω, Keithley 2182A) are connected to obtain the 4-probe differential voltage on each PRT as V/i_{ac}.

is transferred to the adjacent sensing membrane and PRT through parallel mechanisms: (i) through the nanostructure, (ii) through the thermal sink (the silicon substrate), and (iii) through radiation and residual gas conduction. Mechanisms (ii) and (iii) are denoted background thermal conductance, G_{bg}. The uncertainty arising from the thermal radiation contributes less than 2% to the thermal conductance of the beam and sample over 30 to 400 K.[43] At 10^{-8} mbar and 300 K, the thermal conductivity of air is on the order of 10^{-7} W/(m·K) (see Figure S1 of the supplementary material) and contributes a thermal conductance of less than 5 pW/K which accounts for 1.5% of the total G_{bg}. The additional source of uncertainty in this technique, the ambient temperature stability of the cryostat, was measured at better than 2 mK (Figure S2 of the supplementary material).

During the thermal conductance measurement, both of the PRTs serve as thermometers to measure the temperature rise on each suspended membrane, which is determined by the PRTs' temperature-dependent electrical resistance and their temperature coefficient of resistance (TCR) using two Keithley 6221 + 2182A Delta-mode systems. The electrical resistances of the heating membrane PRT and each Pt lead are denoted as R_h and R_L, respectively. A Joule heat, $Q_h = I_{dc}^2 R_h$, is generated when a DC current I_{dc} passes through the heating membrane and causes its temperature to rise from the ambient temperature, T_0 to T_h. Meanwhile, the two current-carrying Pt leads generate and dissipate Joule heat, $2Q_L = 2I_{dc}^2 R_L$, due to the DC current. Uniform temperature on the heating membrane is a justified assumption since the internal thermal resistance of the PRT is two orders of magnitude smaller than

the thermal resistance of the six long Pt leads connecting it to the silicon chip at ambient temperature T_0.[43] A certain portion of the Joule heat, Q_s, is transferred from the heating membrane through the nanostructure to the sensing membrane. The sensing membrane temperature is raised from T_0 to T_s which is assumed to be spatially uniform by the previous justification. This amount of heat is then conducted to the silicon heat sink at T_0 through the six beams supporting the sensing membrane. As energy is conserved, the remaining heat, $Q_1 = Q_h + 2Q_L - Q_s$, is conducted to the silicon chip through the six beams supporting the heating membrane. The thermal conductance of the six beams supporting each membrane, G_b, and the total sample thermal conductance from the heating membrane to the sensing membrane, G_s, are determined with the thermal circuit in Figure 1 as

$$G_b = \frac{1}{R_b} = \frac{Q_h + Q_L}{\Delta T_h + \Delta T_s} \text{ and} \tag{1}$$

$$G_s = \frac{Q_s}{\Delta T_h - \Delta T_s} = G_b \frac{\Delta T_s}{\Delta T_h - \Delta T_s}, \text{ respectively.} \tag{2}$$

The temperature of heating membrane and sensing membrane, T_h and T_s, respectively, is accurately determined by a DC reversal 4-point differential electrical resistance measurement, as depicted in Figure 1. The DC reversal system (Keithley 6221 + 2182A) performs a resistance measurement with following steps:[41] (i) The 2182A nanovoltmeter triggers the 6221 current source to provide a small positive current to the PRT (1.5 μA), (ii) the 6221 sends a trigger signal to the 2182A after an operator-defined current delay time, (iii) the 2182A measures the voltage V_1 with an operator-defined measuring time (number of power line cycles), (iv) the 2182A sends a trigger signal to stop the current source, (v) steps (i) to (iv) are repeated with a small negative current (-1.5 μA) and the voltage V_2 is recorded, (vi) steps (i) to (iv) are repeated again with a positive current and voltage V_3 is recorded, (vii) a three-point moving average algorithm is used to determine the final voltage responses, where $V_{final} = (V_1 - 2V_2 + V_3)/4$. The voltage V_{final} is then associated with the operator-set current, $i_{ac} = 1.5$ μA, to calculate the resistance of the PRT. Schematics of the technique and optimal conditions for this technique are shown in Figures S3–S4 and Table S1 of the supplementary material, respectively.

The change of temperature caused by DC heating results in an electrical resistance change of the PRT which is interpreted back to a temperature rise using the measured TCR of each PRT, $\alpha_i \equiv [\partial R_i(T)/\partial T]/R_i(T)$, i = h, s. To obtain steady-state resistance versus temperature and TCR, we have measured the PRT resistances every ~1 K while the temperature of the chamber was slowly cooled at a rate of 0.1 K/min from 390 to 4 K, as shown in Figure 2. Spikes in α arise from nonlinearities in $R(T)$ that occur randomly during data collection (Figure 2(b)) and likely arise from an unidentified intermittent noise source. The corresponding TCR of each PRT at each ambient temperature point T_0 is used to calculate the temperature change caused by DC joule heating. The TCRs at each T_0 are determined over a temperature range of $T_0 \pm 2$ K to define a local α for use in Eqs. (3) and (4). We note that the regions of noise in α are excluded from our data processing, and the T_0 at which measurements were
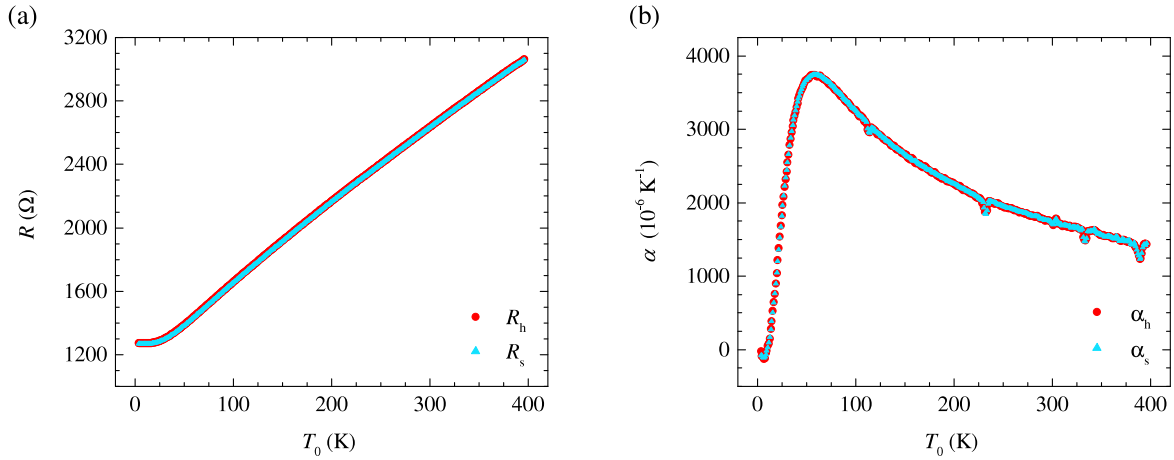
FIG. 2. Electrical resistance, R, and temperature coefficient of resistance (TCR), α, of the heating and sensing PRTs as a function of temperature recorded at the sample mount, T_0. (a) Measured heating and sensing PRT electrical resistances, R_h and R_s, respectively, over a temperature range from 4 to 390 K and (b) the corresponding TCR of heating and sensing PRTs, α_h and α_s, respectively. The TCR at each temperature point is calculated over 5 measured resistance points which correspond to a local temperature range of approximately $T_0 \pm 2$ K.

conducted do not overlap with these problematic regions in the current study. Consequently, the resulting temperature rise on the sensing membrane ΔT_s is a function of the I_{dc} applied on the heating PRT and can be determined as

$$\Delta T_s(I_{dc}) = \frac{1}{\alpha_s}\left(\frac{R_s(I_{dc}) - R_s(I_{dc} = 0)}{R_s(I_{dc} = 0)}\right). \quad (3)$$

Measurement of the temperature rise on the heating membrane is complicated by coupling between AC and DC currents. An AC current i_{ac} with a frequency f_h is coupled to the much larger DC heating current during the electrical resistance measurement and this AC current will generate modulated heating at a frequency of $2f_h$ when f_h is low. Shi et al.[2] have experimentally demonstrated a difference of a factor of 3 between the low frequency and high frequency limits of an unmodulated temperature rise calculation when the DC heating current is coupled with a sinusoidal AC sensing current. The AC and DC coupling effect remains important in the current work because we are employing a square wave AC current in our measurement scheme. A Joule heating, $Q_{ac+dc} = [I_{dc} + i_{ac}(f_h)]^2 R_h$, is generated on the heating membrane by the AC + DC current. This modulated heating will yield a nontrivial component in T_h when the frequency of the AC current is much smaller than $1/(2\pi\tau)$, where τ is the thermal time constant of the suspended microdevice. Thus the measured resistance rise of the heating PRT, ΔR_h, is affected by this AC + DC heating effect in the low frequency regime. Thus the temperature rise ΔT_h is a function of I_{dc} applied on the heating PRT which can be determined as

$$\Delta T_h(I_{dc}) = \frac{1}{\zeta\alpha_h}\left(\frac{R_h(I_{dc}) - R_h(I_{dc} = 0)}{R_h(I_{dc} = 0)}\right),$$
$$\begin{cases} \zeta = 3, & f_h \ll \, ^1/(2\pi\tau) \\ \zeta = 1, & f_h \gg \, ^1/(2\pi\tau) \end{cases}. \quad (4)$$

To investigate the waveform-dependence of the frequency-dependent resistance rise, we have measured the $\Delta R_h(f_h)$ by a lock-in technique using a 1 μA peak-to-peak excitation current in the frequency range from 0.8 Hz to 5.9 kHz for square, sine, and triangle waveforms while DC

heating is applied (Figure 3). The factor ζ does not show a significant change with different types of AC waveforms, where the normalized resistance change due to DC heating $\Delta R_h(f_h)/\Delta R_h(f_h = 1$ Hz$)$ corresponds to $\zeta/3$. Furthermore, the cutoff frequency between the low and high frequency regimes increases with temperature since τ decreases with decreasing temperature. As shown in Figure 4, we observe a higher cutoff frequency at 4 K than 375 K as τ is smaller at 4 K than at 375 K.

We have also compared the resistance rise measured with a DC reversal technique to the resistance rise measured with a lock-in technique (Figure 4). The frequency of the DC reversal technique is based on the current source delay time, nanovoltmeter measuring time (number of power line cycles), and instrument communication time. We have calculated the frequency based on the average measured timestamp, reported twice per period by the instrumentation. The frequency-dependent resistance rise of the DC reversal technique was then used as a reference to determine the cutoff frequency
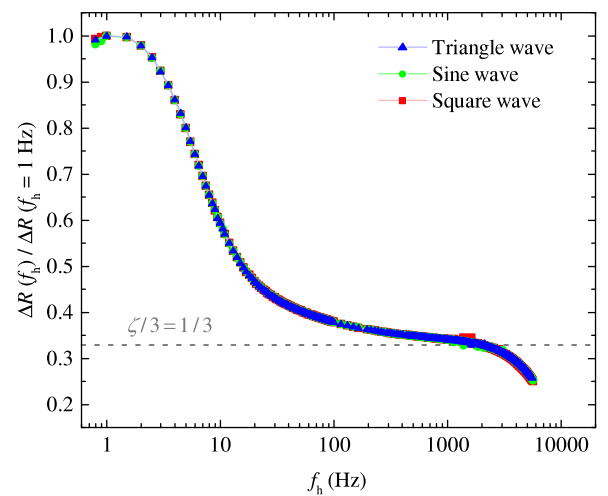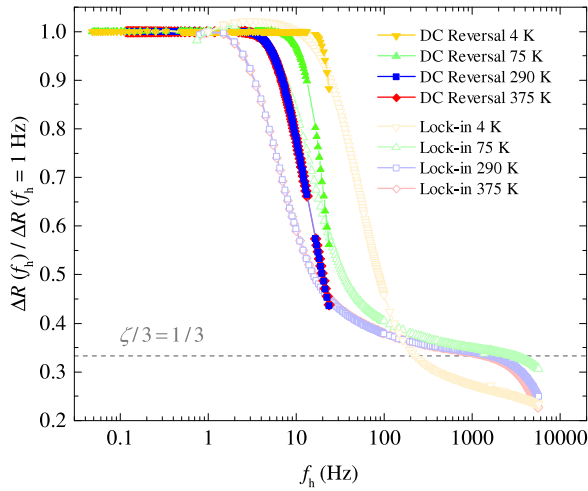

FIG. 3. Normalized first harmonic component of the measured resistance rise of the heating PRT as a function of the frequency of AC current coupled to the DC heating current for different AC waveforms at 290 K. The value of ζ in Eq. (4) is determined by the following relationship, $\zeta = 3\Delta R_h(f_h)/\Delta R_h(f_h = 1$ Hz$)$.

FIG. 4. Normalized first harmonic component of the measured resistance rise of the heating PRT as a function of the frequency of AC current coupled to the DC heating current at 375, 290, 75, and 4 K obtained by the DC reversal technique and by the lock-in technique with square wave excitation. The value of ζ in Eq. (4) is determined by following relationship, $\zeta = 3\Delta R_h(f_h)/\Delta R_h(f_h = 1\ \text{Hz})$.

FIG. 5. Rise in measured resistance of the PRT in units of parts per million caused by self-heating from the AC sensing current, $[R(i_{ac}) - R(i_{ac} = 0.3\ \mu\text{A})]/R(i_{ac} = 0.3\ \mu\text{A})$, as a function of AC sensing current amplitude at 22.37 Hz. The measured standard derivation of the resistance, $\sigma/R(i_{ac})$, is shown for comparison in units of parts per million. We have determined an optimal i_{ac} of 1.5 μA peak-to-peak for the DC reversal technique based on minimizing noise while maintaining an acceptably small resistance rise corresponding to 71.6 mK.

defined as $\Delta R_h(f_h)/\Delta R_h(f_h = 1\ \text{Hz}) = 0.998$, which is 12.94, 6.39, 3.02, and 2.97 Hz at 4, 75, 290, and 375 K, respectively. As our technique is designed for use in the low frequency regime, we determine 3 Hz is appropriate over the full temperature range of 4–375 K, ensuring $\zeta = 3$ in Eq. (4).

III. TEMPERATURE AND BACKGROUND THERMAL CONDUCTANCE RESOLUTION

Resistance-based thermometry is based on temperature-dependent electrical resistance, so that the measured resistance can be correlated with the temperature of the object to which the PRT is attached. On the sensing membrane, where only an AC signal is used in the resistance measurement, Eq. (3) can be used to convert the measured change in resistance to a change in temperature. Thus, the noise equivalent temperature of the sensing PRT (NET$_s$) is calculated based on Eq. (3) and the lowest total voltage noise in the electrical resistance measurement, ΔV_{noise}, as

$$\text{NET}_s = \Delta T_{\text{Resolution}} = \frac{\Delta V_{noise}}{\alpha i_{ac} R_s(T)}. \quad (5)$$

Improving NET$_s$ can be achieved by employing a larger resistance PRT and larger sensing current. However, self-heating is detrimental to the measurement when the sensing current is too high (Figure 5). Thus, lowering ΔV_{noise} is a more appropriate strategy to enhance the temperature resolution of suspended micro-thermometry technique. Contributions to the voltage noises are categorized as intrinsic noises (Johnson and shot noises) and non-intrinsic noises (1/f noise, temperature drift, etc.). In this experiment, the total noise in the voltage signal can be estimated as

$$\Delta V_{noise}^2 = \Delta V_{\text{electrical}}^2 + \Delta V_{\text{temperature drift}}^2, \quad (6)$$

where $\Delta V_{\text{electrical}}^2$ is the mean square of electrical noises arising from the intrinsic noises of resistance and the non-
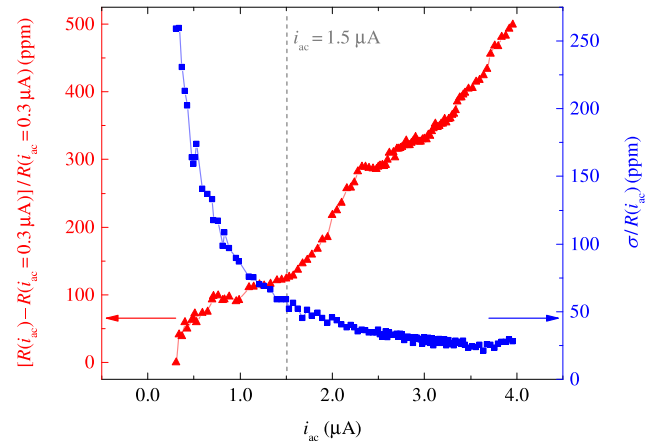
intrinsic noise from the instrumentation, and $\Delta V_{\text{temperature drift}}^2$ is the measured mean square voltage noise due the ambient temperature drift of the sample mount.

Use of a larger AC sensing current, i_{ac}, is a separate strategy to lower the noise equivalent temperature as per Eq. (5), as well as the noise equivalent conductance, without contributing substantial modulated heating. We have measured the PRT resistance and its noise (ppm, $[\sigma/R(i_{ac})] \cdot 10^6$) as a function of sensing current from 0.3 μA to 5 μA (Figure 5). The electrical resistance of the PRT does not show a significant increase with a sensing current between 0.3 and 1.5 μA, indicating a negligible self-heating effect on the suspended membrane. In contrast, the standard derivation of measured resistance dramatically decreases with increasing i_{ac}. In other words, the noises contributed from the electrical measurement can be minimized by applying a higher AC current, but this will also induce non-negligible self-heating. We calculated the temperature rise with $i_{ac} = 1.5\ \mu$A as ∼70 mK. Nevertheless, the rise of resistance due to AC current heating is a constant offset which will cancel out during the calculation of $\Delta R_i(I_{dc}) = R_i(I_{dc}) - R_i(I_{dc} = 0)$, $i = $ h, s on each suspended membrane. To examine the effect of AC self-heating on the heat flow measurement, we have measured the temperature rise ΔT_s on the sensing PRT as a function of DC heating power applied to the heating PRT from 0 to 3000 nW with 0.5, 1.5, 2.5, and 3.5 μA AC excitation currents at $f_s = 22.37$ Hz (Figure 6). The ΔT_s measured with 1.5 μA or higher AC excitation current offers three times better temperature resolution than 0.5 μA and does not show a significant self-heating effect. Thus we have chosen 1.5 μA as the optimal AC excitation current to measure the NET$_s$ in this work as this current exhibits roughly the same temperature resolution as the higher currents shown in Figure 6.

In order to determine NET$_s$, we first identify the noise components of ΔV_{noise}. The major advantage of the DC reversal technique is that it can diminish 1/f noises and noise due
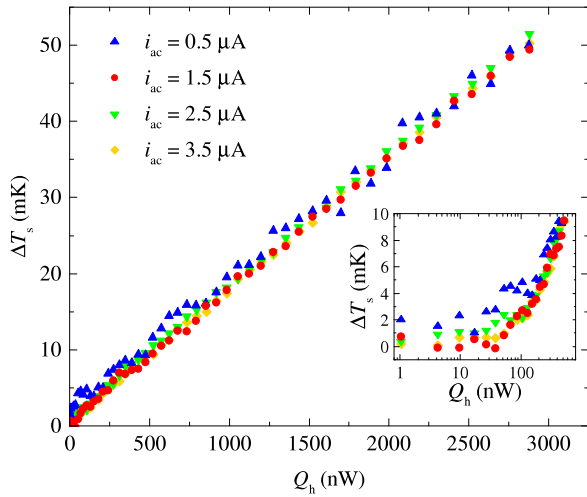
FIG. 6. Measured sensing PRT temperature rise as a function of $Q_h = I_{dc}^2 R_h$, shown for varied AC excitation currents ($f_s = 22.37$ Hz) of 0.5, 1.5, 2.5, and 3.5 μA and obtained at $T_0 = 375$ K. The inset shows the low Q_h regime; note that 1.5 μA is sufficient to achieve high resolution without inducing a large self-heating effect.

to offsets arising from thermal drift.[41] The common mode rejection ratio (CMRR) of an instrument describes the ability of common noise rejection in the measurement. The DC reversal system (Keithley 6221 + 2182A) has a CMRR of more than 200 dB ($V_{signal} \pm V_{noise}/10^{10}$), which is extremely high in comparison to high-resolution lock-in amplifiers which only have a CMRR of 100 dB (Stanford Research Systems SR830, $V_{signal} \pm V_{noise}/10^5$). In other words, the instrumentation used in the DC reversal technique has a much better capability to reject non-intrinsic noises by attenuation of these noises to a value five orders of magnitude smaller than for lock-in amplifiers. In addition, the programmable current source used in this technique has an input impedance of $>10^{14}$ Ω, which provides a stable and load-independent current through the PRTs (we have measured $\delta i_{ac}/i_{ac} \sim 10^{-7}$), effectively

eliminating shot noise. Therefore, the Johnson noise is the dominant contribution to electrical noise and is expressed as

$$\Delta V_{electrical} = \Delta V_{Johnson} = (4k_B T R \Delta f)^{0.5}, \quad (7)$$

where $\Delta f \sim 1$ Hz is the noise equivalent bandwidth for the DC reversal system and k_B is the Boltzmann constant. The NET_s at each ambient temperature point is calculated based on Eqs. (5)–(7). The $NET_{temperature\ drift}$ represents the stability of the cryostat sample mount temperature and is directly obtained as the standard deviation of recorded sample mount temperatures during measurement. A summary of the temperature dependent contributions to NET is shown in Figure 7.

As we have obtained the NET_s of the DC reversal technique, the noise equivalent conductance (NEG) of the suspended microdevice, which is the minimum thermal conductance that can be detected by the suspended device, can be expressed using Eqs. (2) and (5) as

$$NEG = G_b \frac{NET_s}{\Delta T_h - \Delta T_s}, \quad (8)$$

where G_b is the measured thermal conductance of the six beams supporting each membrane. The NET_s and NEG calculated from the above analysis are given in Table S2 of the supplementary material.

IV. MEASUREMENT OF THE BACKGROUND THERMAL CONDUCTANCE

We have measured the background conductance on a bare device to experimentally determine the minimum temperature resolution and minimum thermal conductance resolution of the DC reversal suspended micro-thermometry technique over a temperature range of 30–375 K. During each measurement set, I_{dc} is applied to the heating membrane at discrete values from 0 to $+I_{dc,max}$ to $-I_{dc,max}$ and back to 0. At each I_{dc} value, the average of 20 electrical resistance measurements
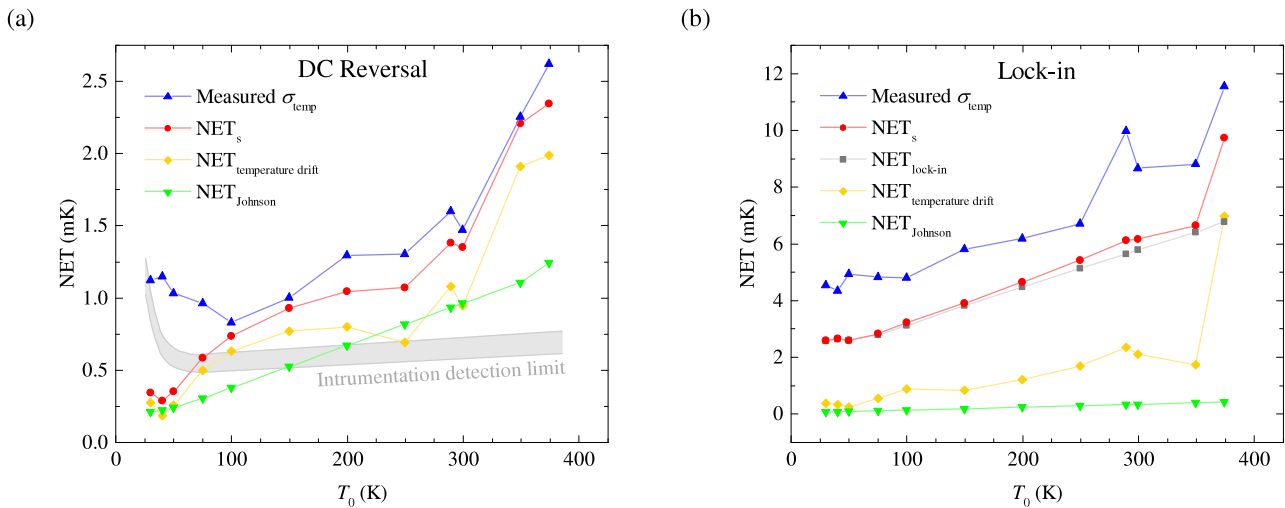

FIG. 7. (a) Temperature dependence of contributions to the sensing noise equivalent temperature (NET_s) of the DC reversal technique ($NET_{temperature\ drift}$ and $NET_{Johnson}$), shown in comparison to the total (pooled) standard deviation of the measured temperature rise, σ_{temp}, and the calculated delta mode instrumentation detection limit based on minimum resolution of 4.2–5 nV and Eq. (5). (b) Temperature dependence of contributions to the sensing noise equivalent temperature (NET_s) of the lock-in technique ($NET_{temperature\ drift}$, $NET_{Johnson}$, and $NET_{lock-in}$), shown in comparison to the total (pooled) standard deviation of the measured temperature rise, σ_{temp}.
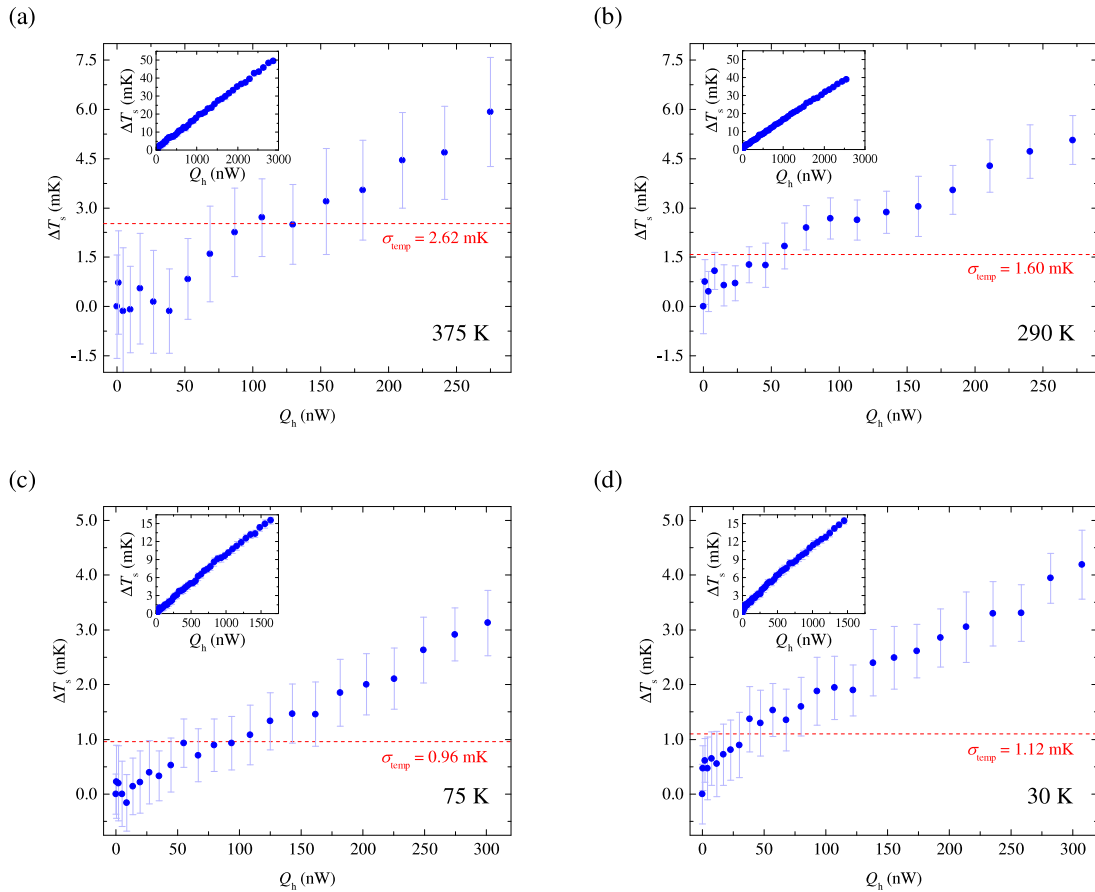
FIG. 8. Measured temperature rise on the sensing PRT, ΔT_s, as a function of heating power Q_h detected using the DC reversal technique with a 1.5 μA AC excitation current at 22.37 Hz. T_0 = (a) 375 K, (b) 290 K, (c) 75 K, and (d) 30 K. Error bars are defined as one standard deviation of $\Delta T_s(Q_h)$ over five separate measurement sets (one set is defined as $I_{dc} = 0$ to $-I_{dc,max}$ to $+I_{dc,max}$ to 0). The measured total (pooled) standard deviation of the temperature rise, σ_{temp}, is shown for comparison at each T_0.

of $\Delta R_h(I_{dc})$ and the average of 200 measurements of $\Delta R_s(I_{dc})$ are taken to determine $\Delta T_h(I_{dc})$ and $\Delta T_s(I_{dc})$, respectively. The difference in number of data points ensures that both measurements are completed at roughly the same time, as f_h = 3 Hz and f_s = 22.37 Hz.

Figure 8 shows the measured temperature rise on the sensing membrane, ΔT_s, as a function of heating power, Q_h, at different ambient temperatures. The average and standard derivation of ΔT_s is calculated based on five measurement sets at each heating power. In order to obtain statistics on the uncertainty of the entire measurement, the overall standard derivation of temperature rise, σ_{temp}, is computed as a pooled standard deviation estimation from different populations.[44] The twenty measured $\Delta T_s(Q_h)$ at each heating power were considered as one statistical population and the error bars in Figure 8 are defined to have a magnitude of one standard deviation of this population. As we have used the same instruments throughout the entire experiment, the overall (pooled) standard derivation of all the measured temperature rises was calculated as

$$\sigma_{temp} = \sqrt{\frac{\sum_{i=1}^{k}(n_i - 1)\sigma_i^2}{\sum_{i=1}^{k} n_i - 1}}, \qquad (9)$$

where σ_i and n_i are the sample standard derivation and sample size of the measured temperature rise at each heating power. The DC reversal method exhibits sensing temperature resolution of 2.62 mK, 1.60 mK, 0.96 mK, and 1.12 mK at ambient sample temperatures of T_0 = 375 K, 290 K, 75 K, and 30 K, respectively. This is slightly higher than the NET_s given in Figure 7(a) and Table S2 of the supplementary material. Thus, the temperature resolution is limited by the DC reversal measurement instrumentation which has a voltage resolution of ~4.2–5 nV. This yields $NET_{instrumentation\ limit}$ = 0.65 − 0.74 mK. In other words, 0.65–0.74 mK is the smallest temperature which this system can measure regardless of the NET_s. Impressively, the temperature resolution of this technique is able to achieve 1 mK without using complicating schemes such as a matching resistance or a Wheatstone bridge circuit to cancel the temperature drift. This prevents the need for complicated calibration processes, multiple measurement schemes, and laborious data analysis and enables high-throughput measurement of the thermal conductance of individual nanostructures. We note that the instrumentation limit of the voltage detection inputs of the lock-in amplifier corresponds to ~7 μK assuming a Wheatstone bridge is used to allow the maximum amplification range of 1 nV; however, this is not observable as the voltage source noise dominates in the lock-in method ($NET_{lock-in}$, Figure 7(b)).
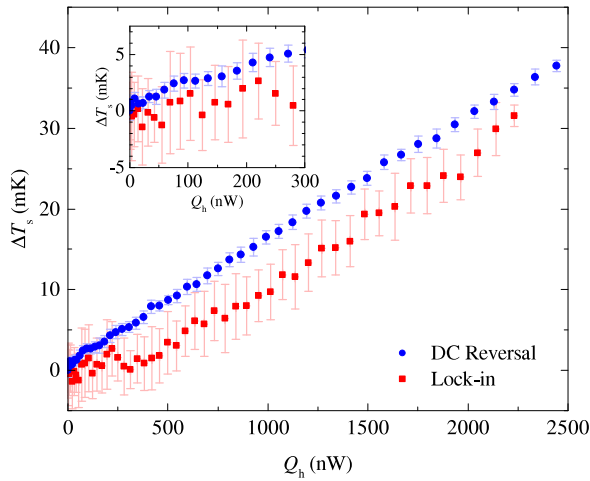
FIG. 9. Measured sensing PRT temperature rise, ΔT_s, as a function of heating power, Q_h, at ambient temperature $T_0 = 290$ K. The DC reversal technique is measured using a 1.5 μA AC excitation current at $f_s = 22.37$ Hz. The lock-in technique is measured using a 1.5 μA (peak-to-peak) AC excitation current at $f_s = 199.03$ Hz and a 1 MΩ precision resistor to convert the lock-in amplifier internal voltage source to a current. The total (pooled) standard deviation of the temperature rise measured by the lock-in is $\sigma_{temp} = 9.38$ mK while that of DC reversal technique is an order of magnitude lower at 1.59 mK.

We have also compared the DC reversal technique to the lock-in technique, as shown in Figures 9–11. The scheme we have used is similar to that of Ref. 2; however, with a larger AC sensing current of $i_{ac} = 1.5$ μA, provided using 1.5 $V_{peak-to-peak}$ across a 1 MΩ high precision resistor (Caddock USF370-1.00M-0.01%-5 ppm). The temperature resolution of the DC reversal technique is 5.9 times smaller than the lock-in technique at 290 K because the lock-in method has additional noise contributions from the voltage source of the amplifier, the voltage to current converter, and shot noise. The NET due to these components of the lock-in technique can be expressed as

$$\text{NET}_{\text{lock-in}} = \left(\frac{\Delta V_{ac}}{V_{ac}} + \frac{\Delta R}{R} + \frac{\Delta i_{ac}}{i_{ac}} \right) \Big/ \alpha_s, \qquad (10)$$

where ΔV_{ac}, ΔR, and Δi_{ac} are the lock-in voltage source noise, noise from resistor used to convert voltage to current, and current noise, respectively. The voltage source noise component ($\Delta V_{ac}/V_{ac}$) contributes 90.1% of the total $\text{NET}_{\text{lock-in}}$, while the resistor uncertainty ($\Delta R/R$) contributes ~9%. As can be seen in Figure 7(b), these sources of noise dominate over temperature drift and Johnson noise. In addition, the SR830 lock-in amplifier has a relatively poor common mode noise rejection (CMNR) in comparison to the DC reversal instrumentation. A reduced number of noise sources and improvement of the CMNR of the DC reversal system allow us to achieve the demonstrated improvement in resolution. The NET_s can be further improved if a matching resistance or Wheatstone bridge is incorporated to cancel the temperature drift, and the addition of differential amplifiers that have the same order of CMNR as the DC reversal instrumentation. However, we note that the matching resistance, Wheatstone bridge, or the differential amplifiers would contribute non-intrinsic noises to the measurement system as well as increase the experimental complexity by requiring each measurement to be calibrated and hence would void the high-throughput design of our technique.

The resolution of thermal conductance is also substantially improved using the DC reversal technique. Based on five measurement sets at ambient temperature $T_0 = 375$, 290, 75, and 30 K, the measured thermal background conductance is $G_{bg} = 528.09, 370.54, 90.91$, and 47.97 pW/K, and the standard derivation of G_{bg} is $\sigma_{Gbg} = 26.42$ pW/K, 13.54 pW/K, 6.16 pW/K, and 1.73 pW/K, respectively. As standard deviation of the measurement is on the order of NEG, we have confidence that we have reached the maximum thermal conductance resolution of this technique, corresponding to the instrumentation limit.

In comparison with G_b measured by the DC reversal technique, where $\zeta = 3$ in Eq. (4), the G_b and G_{bg} measured at 290 K by the lock-in method are 1.92%–6.62% and 3.37%–23.80% lower, respectively (Figures 10–11). This is a significant unreported uncertainty of the lock-in technique, where at high frequencies, $\zeta \neq 1$ (see Figures 3–4) as is
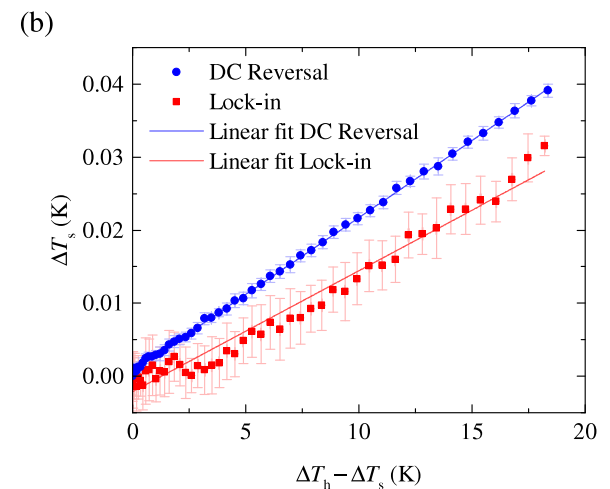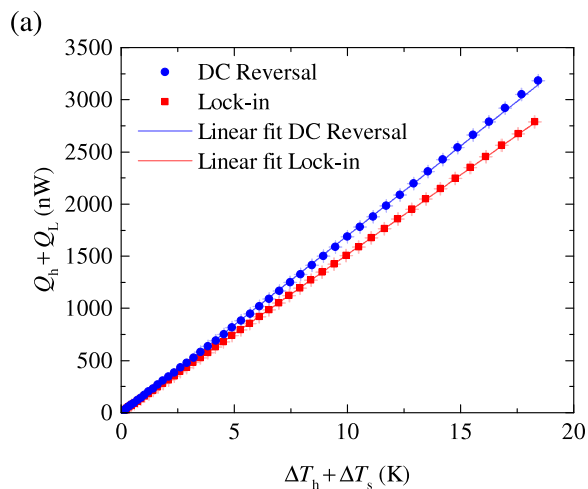

FIG. 10. (a) Total heat conducted through the six beams supporting the heating membrane to the environment at $T_0 = 290$ K; the slope of $Q_h + Q_L$ as a function of $\Delta T_h + \Delta T_s$ yields G_b. (b) Corresponding temperature rise on the sensing membrane, ΔT_s as a function of $\Delta T_h - \Delta T_s$; the slope yields the ratio of G_b/G_s.
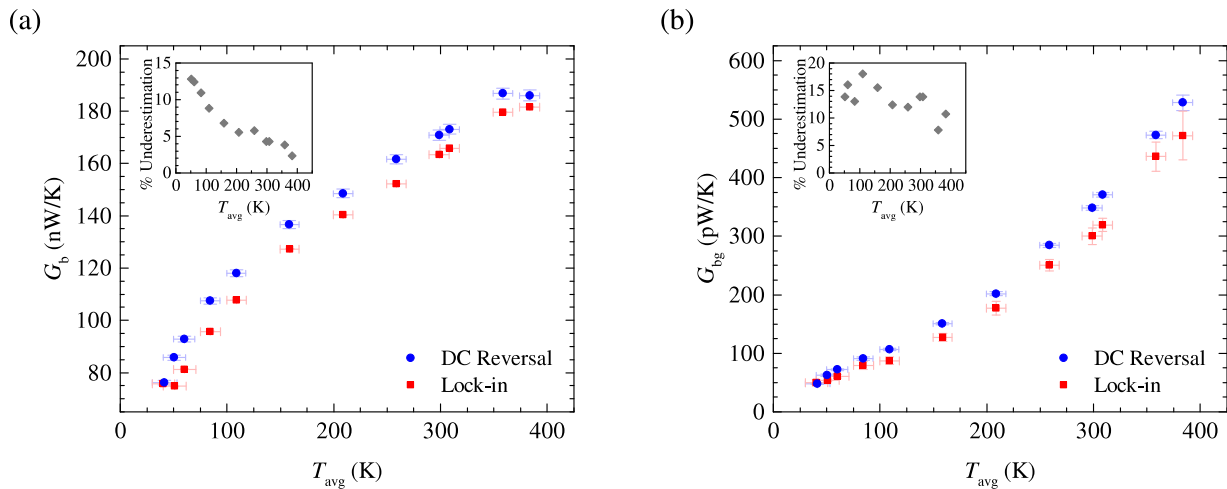
FIG. 11. (a) Measured beam conductance, G_b, at different average temperatures, T_{avg}. The uncertainty of G_b is better than 2.2% within a 20 K temperature range for both the DC reversal and lock-in techniques. (b) Measured background thermal conductance, G_{bg}, at different average temperatures, T_{avg}. The uncertainty in G_{bg} is on the order of ~2.47%–6.75% within a 20 K temperature range for the DC reversal technique. This is an impressive improvement over the traditional lock-in-based technique which exhibits an uncertainty in G_{bg} of ~8.5%–21%. Additionally, the lock-in-based technique obtains a 2.37%–12.80% underestimation of G_b and a 7.80%–18.04% underestimation of G_{bg} when compared to the DC reversal technique. This is attributed to $\zeta \neq 1$ (see Figures 3–4) at high frequencies where a value of 1 is assumed. The percent underestimation in G_b and G_{bg} is calculated as $100 \cdot (G_{DC\ reversal} - G_{lock-in})/G_{DC\ reversal}$.

commonly assumed. An additional complication is that the actual value of ζ is a function of temperature in the high frequency regime as shown in Figure 4. Assuming $\Delta T_h \gg \Delta T_s$, this leads to an overestimation of ΔT_h by a factor of $1/\zeta$ according to Eq. (4) and a corresponding underestimation in G_b by a factor of ζ. Similarly, G_b/G_s is underestimated by a factor of ζ based on Eq. (2), and the calculated G_s is then underestimated by a factor of ζ^2. At 290 K, we have measured $\zeta(f = 747.7\ \text{Hz}) = 1.043$. With respect to the DC reversal technique, we have measured a corresponding underestimation of G_b by 1.92%–6.62% and a corresponding underestimation of G_{bg} by 3.37%–23.80% when using the lock-in technique. This is in agreement with the 4.3% underestimation in G_b and the 9.1% underestimation in G_{bg}, predicted based on the measured value of ζ. This problem is remedied using the DC reversal technique which is stable at very low frequencies where the value of ζ is uniquely 3.

V. CONCLUSIONS

In summary, we have developed a new resistance thermometry measurement technique benefitting from improved common mode noise rejection over traditional lock-in amplifier-based techniques. This DC reversal technique offers a high throughput and simple measurement scheme with ~1.6 mK temperature resolution and ~14 pW/K thermal conductance resolution at 290 K. Given these results, the DC reversal technique combined with suspended micro-thermometry will enable fundamental studies of phonon transport in nanoscale materials where both high throughput and high resolution are required.

SUPPLEMENTARY MATERIAL

See supplementary material for detailed experimental setup and resolution data.

[1]P. Kim, L. Shi, A. Majumdar, and P. L. McEuen, Phys. Rev. B **87**, 215502 (2001).
[2]L. Shi, D. Li, C. Yu, W. Jang, D. Kim, Z. Yao, P. Kim, and A. Majumdar, J. Heat Transfer **125**, 881 (2003).
[3]J. Hone, B. Batlogg, Z. Benes, A. T. Johnson, and J. E. Fischer, Science **289**, 1730 (2000).
[4]E. Pop, D. Mann, Q. Wang, K. Goodson, and H. Dai, Nano Lett. **6**, 96 (2006).
[5]I.-K. Hsu, R. Kumar, A. Bushmaker, S. B. Cronin, M. T. Pettes, L. Shi, T. Brintlinger, M. S. Fuhrer, and J. Cumings, Appl. Phys. Lett. **92**, 063119 (2008).
[6]I.-K. Hsu, M. T. Pettes, M. Aykol, C.-C. Chang, W.-H. Hung, J. Theiss, L. Shi, and S. B. Cronin, J. Appl. Phys. **110**, 044328 (2011).
[7]D. Li, Y. Wu, P. Kim, L. Shi, P. Yang, and A. Majumdar, Appl. Phys. Lett. **83**, 2934 (2003).
[8]J. Zhou, C. Jin, J. H. Seol, X. Li, and L. Shi, Appl. Phys. Lett. **87**, 133109 (2005).
[9]A. Boukai, K. Xu, and J. R. Heath, Adv. Mater. **18**, 864 (2006).
[10]A. L. Moore, M. T. Pettes, F. Zhou, and L. Shi, J. Appl. Phys. **106**, 034310 (2009).
[11]A. Mavrokefalos, A. L. Moore, M. T. Pettes, L. Shi, W. Wang, and X. Li, J. Appl. Phys. **105**, 104318 (2009).
[12]J. Kim, S. Lee, Y. M. Brovman, P. Kim, and W. Lee, Nanoscale **7**, 5053 (2015).
[13]S. Shen, A. Henry, J. Tong, R. Zheng, and G. Chen, Nat. Nanotechnol. **5**, 251 (2010).
[14]V. Singh, T. L. Bougher, A. Weathers, Y. Cai, K. Bi, M. T. Pettes, S. A. McMenamin, W. Lv, D. P. Resler, T. R. Gattuso, D. H. Altman, K. H. Sandhage, L. Shi, A. Henry, and B. A. Cola, Nat. Nanotechnol. **9**, 384 (2014).
[15]A. Weathers, Z. U. Khan, R. Brooke, D. Evans, M. T. Pettes, J. W. Andreasen, X. Crispin, and L. Shi, Adv. Mater. **27**, 2101 (2015).
[16]C. Chiritescu, D. G. Cahill, N. Nguyen, D. Johnson, A. Bodapati, P. Keblinski, and P. Zschack, Science **315**, 351 (2007).
[17]A. Mavrokefalos, Q. Lin, M. Beekman, J. H. Seol, Y. J. Lee, H. Kong, M. T. Pettes, D. C. Johnson, and L. Shi, Appl. Phys. Lett. **96**, 181908 (2010).

[18]A. A. Balandin, S. Ghosh, W. Bao, I. Calizo, D. Teweldebrhan, F. Miao, and C. N. Lau, Nano Lett. **8**, 902 (2008).

[19]J. H. Seol, I. Jo, A. L. Moore, L. Lindsay, Z. H. Aitken, M. T. Pettes, X. Li, Z. Yao, R. Huang, D. Broido, N. Mingo, R. S. Ruoff, and L. Shi, Science **328**, 213 (2010).

[20]R. Yan, J. R. Simpson, S. Bertolazzi, J. Brivio, M. Watson, X. Wu, A. Kis, T. Luo, A. R. Hight Walker, and H. G. Xing, ACS Nano **8**, 986 (2014).

[21]I. Jo, M. T. Pettes, E. Ou, W. Wu, and L. Shi, Appl. Phys. Lett. **104**, 201902 (2014).

[22]I. Jo, M. T. Pettes, J. Kim, K. Watanabe, T. Taniguchi, Z. Yao, and L. Shi, Nano Lett. **13**, 550 (2013).

[23]J. Yang, Y. Yang, S. W. Waltermire, X. Wu, H. Zhang, T. Gutu, Y. Jiang, Y. Chen, A. A. Zinn, R. Prasher, T. T. Xu, and D. Li, Nat. Nanotechnol. **7**, 91 (2012).

[24]Z. Wang, R. Xie, C. T. Bui, D. Liu, X. Ni, B. Li, and J. T. L. Thong, Nano Lett. **11**, 113 (2011).

[25]G. Chen and A. Shakouri, J. Heat Transfer **124**, 242 (2001).

[26]M. F. L. De Volder, S. H. Tawfick, R. H. Baughman, and A. J. Hart, Science **339**, 535 (2013).

[27]L. Shi, C. Dames, J. R. Lukes, P. Reddy, J. Duda, D. G. Cahill, J. Lee, A. Marconnet, K. E. Goodson, J.-H. Bahk, A. Shakouri, R. S. Prasher, J. Felts, W. P. King, B. Han, and J. C. Bischof, Nanoscale Microscale Thermophys. Eng. **19**, 127 (2015).

[28]A. A. Balandin, Nat. Mater. **10**, 569 (2011).

[29]S. Z. Butler, S. M. Hollen, L. Cao, Y. Cui, J. A. Gupta, H. R. Gutiérrez, T. F. Heinz, S. S. Hong, J. Huang, A. F. Ismach, E. Johnston-Halperin, M. Kuno, V. V. Plashnitsa, R. D. Robinson, R. S. Ruoff, S. Salahuddin, J. Shan, L. Shi,

M. G. Spencer, M. Terrones, W. Windl, and J. E. Goldberger, ACS Nano **7**, 2898 (2013).

[30]J. Kim, E. Ou, D. P. Sellan, and L. Shi, Rev. Sci. Instrum. **86**, 044901 (2015).

[31]S. Chen, Q. Wu, C. Mishra, J. Kang, H. Zhang, K. Cho, W. Cai, A. A. Balandin, and R. S. Ruoff, Nat. Mater. **11**, 203 (2012).

[32]K. E. Goodson and Y. S. Ju, Annu. Rev. Mater. Sci. **29**, 261 (1999).

[33]T. Kodama, A. Jain, and K. E. Goodson, Nano Lett. **9**, 2005 (2009).

[34]M. T. Pettes, H. Ji, R. S. Ruoff, and L. Shi, Nano Lett. **12**, 2959 (2012).

[35]A. K. Vallabhaneni, D. Singh, H. Bao, J. Murthy, and X. Ruan, Phys. Rev. B **93**, 125432 (2016).

[36]V. V. Deshpande, S. Hsieh, A. W. Bushmaker, M. Bockrath, and S. B. Cronin, Phys. Rev. Lett. **102**, 105501 (2009).

[37]S. Sadat, E. Meyhofer, and P. Reddy, Rev. Sci. Instrum. **83**, 084902 (2012).

[38]A. Weathers, K. Bi, M. T. Pettes, and L. Shi, Rev. Sci. Instrum. **84**, 084903 (2013).

[39]J. Zheng, M. C. Wingert, E. Dechaumphai, and R. Chen, Rev. Sci. Instrum. **84**, 114901 (2013).

[40]S. Sadat, E. Meyhofer, and P. Reddy, Appl. Phys. Lett. **102**, 163110 (2013).

[41]A. Daire, W. Goeke, and M. A. Tupta, Keithley Instruments, Inc., 2005, http://www.tek.com/sites/tek.com/files/media/document/resources/Lock-In%20WP.pdf.

[42]M. T. Pettes and L. Shi, Adv. Funct. Mater. **19**, 3918 (2009).

[43]A. L. Moore and L. Shi, Meas. Sci. Technol. **22**, 015103 (2011).

[44]R. M. Bethea, *Statistical Methods for Engineers and Scientists* (CRC Press, Boca Raton, FL, 1995), p. 672, ISBN: 9780824793357, https://www.crcpress.com/Statistical-Methods-for-Engineers-and-Scientists-Third-Edition/Bethea/9780824793357 .

Ultra-high resolution steady-state micro-thermometry using a bipolar direct current reversal technique

Jason Yingzhi Wu, Wei Wu, and Michael Thompson Pettes[*]

Department of Mechanical Engineering and Institute of Materials Science, University of Connecticut, Storrs, CT 06269, USA

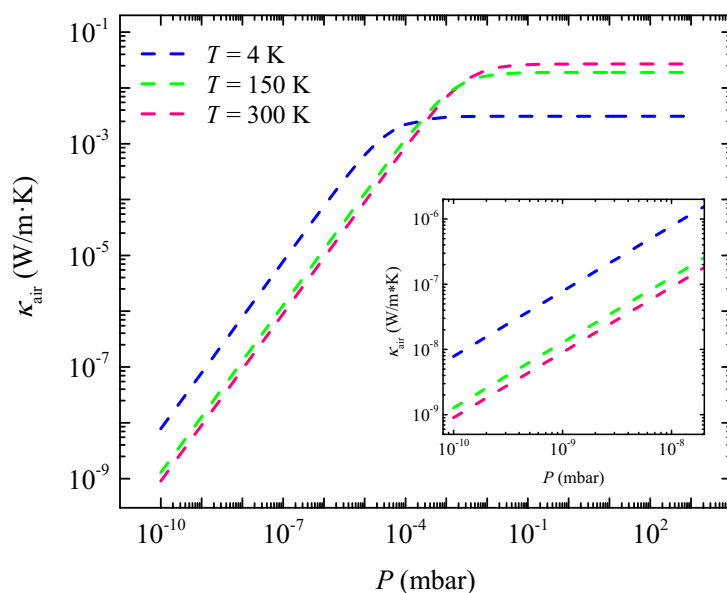[*]Author to whom correspondence should be addressed: michael.pettes@uconn.edu

Figure S1. *Kinetic theory calculation of the thermal conductivity of residual air molecules, κ_{air}, inside an enclosure chamber with a diameter of 2.5 inches (~ sample chamber diameter) as a function of pressure, P, from 10^{-10} to 1000 mbar at certain ambient chamber temperature (T = 4, 150, and 300 K) by kinetic theory of gases. inset shows corresponded air thermal conductivity within cryostat chamber pressure range (10^{-10} to 10^{-8} mbar).*
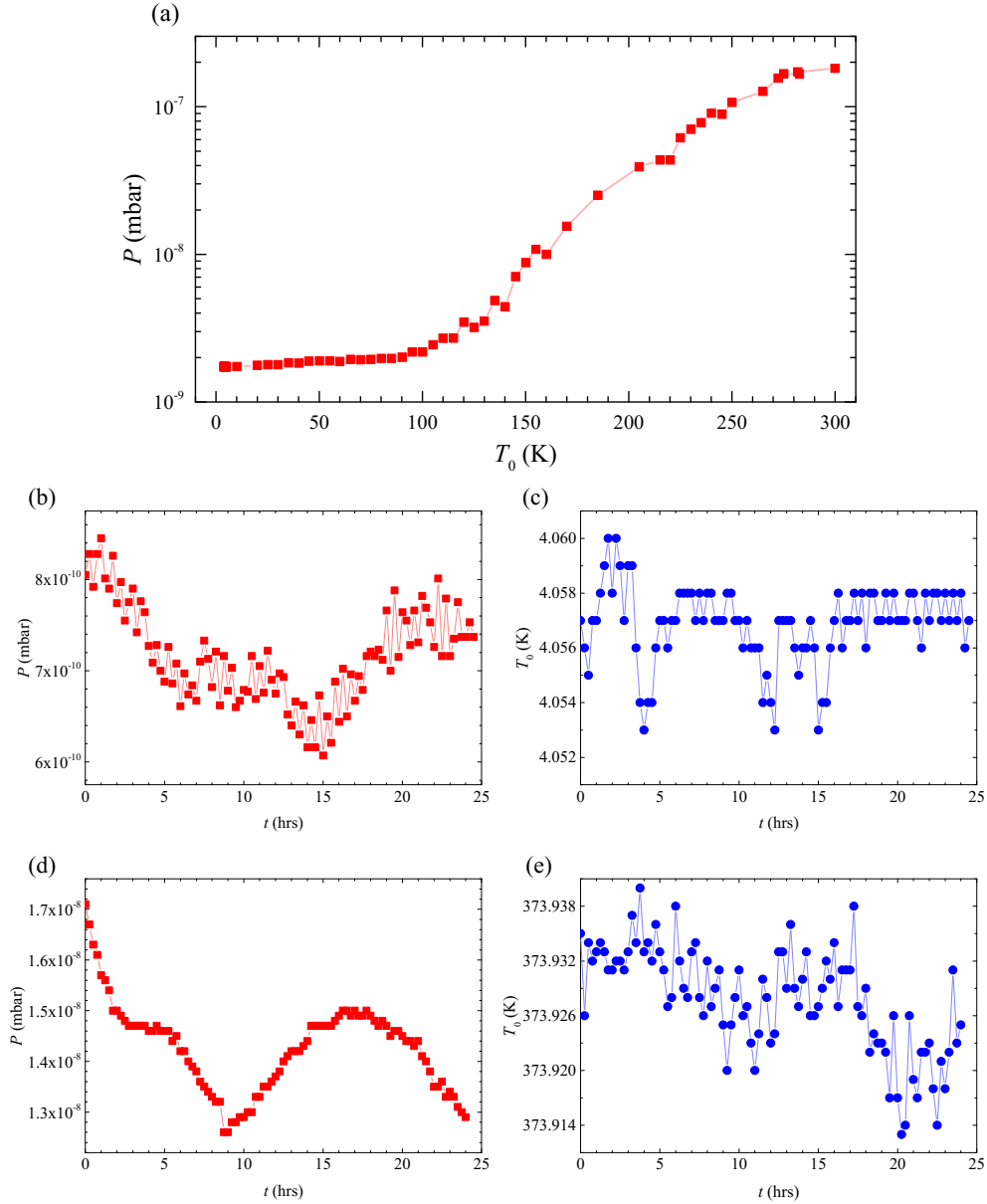
Figure S2. *(a) Ultra high vacuum cryostat chamber pressure as a function of temperature recorded at the sample mount, T_0 over a temperature range from 4 to 300 K. (b) Measured cryostat chamber pressure as a function of time at 4 K sample mount temperature, the system maintained vacuum better than 8.5×10^{-10} mbar over 24 hours. (c) Measured cryostat sample mount temperature as a function of time at 4 K, it maintained a stability better than 1 mK over 24 hours. (d) Measured cryostat chamber pressure as a function of time at 375 K sample mount temperature, it maintained vacuum better than 1.5×10^{-8} mbar over 24 hours. (e) Measured cryostat sample mount temperature as a function of time at 375 K, it maintained a stability better than 20 mK over 24 hours. Data depicted in (b) and (c) were collected while the temperature of the heater was set at 4.0000 K, (e) and (f) were collected while the temperature of heater was set at 375.000 K. The temperature drift in the thermal conductance measurement was much smaller than above data because each measurement set was taken within 0.5 hours.*
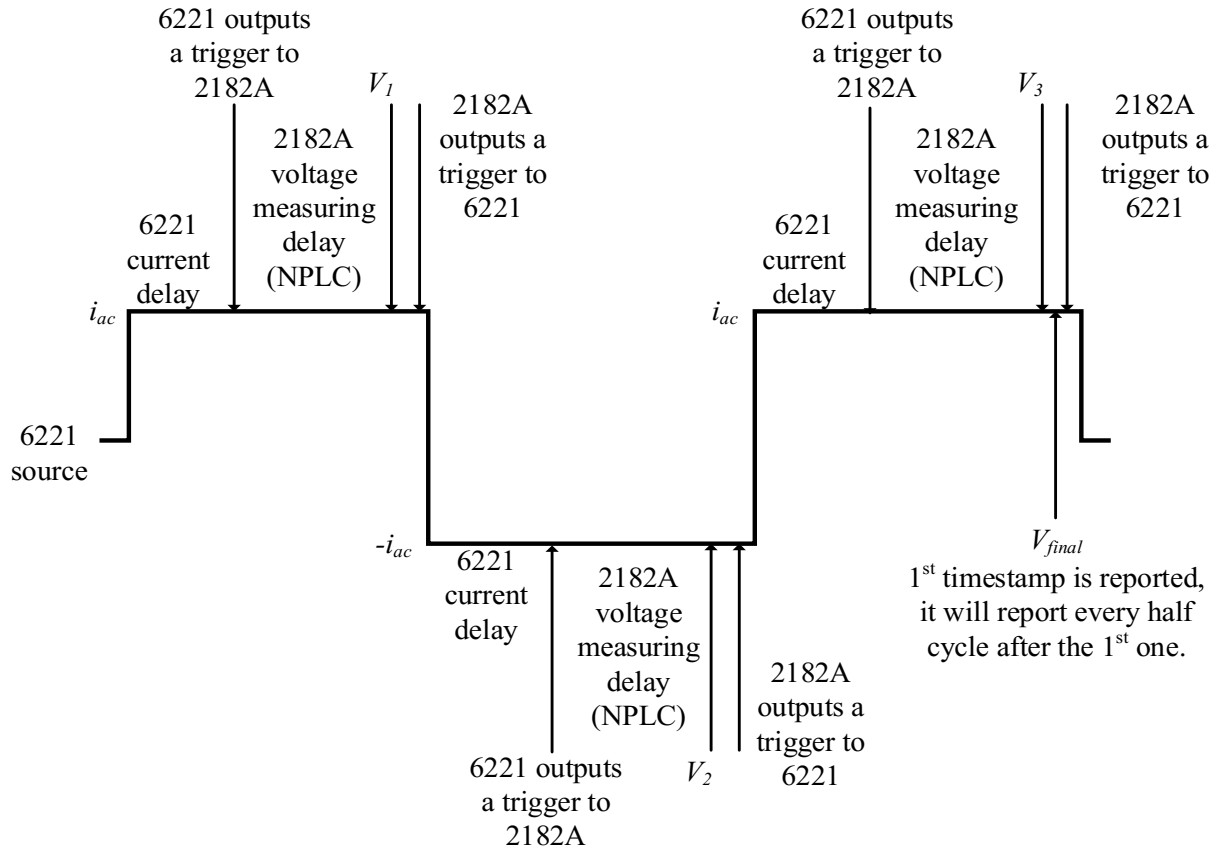
Figure S3. *Schematic of the Keithley 6221 current source and Keithley 2182A nanovoltmeter DC reversal measurement technique (Delta Mode) data processing. The time period is not shown to scale. Adapted from Ref. S1.*
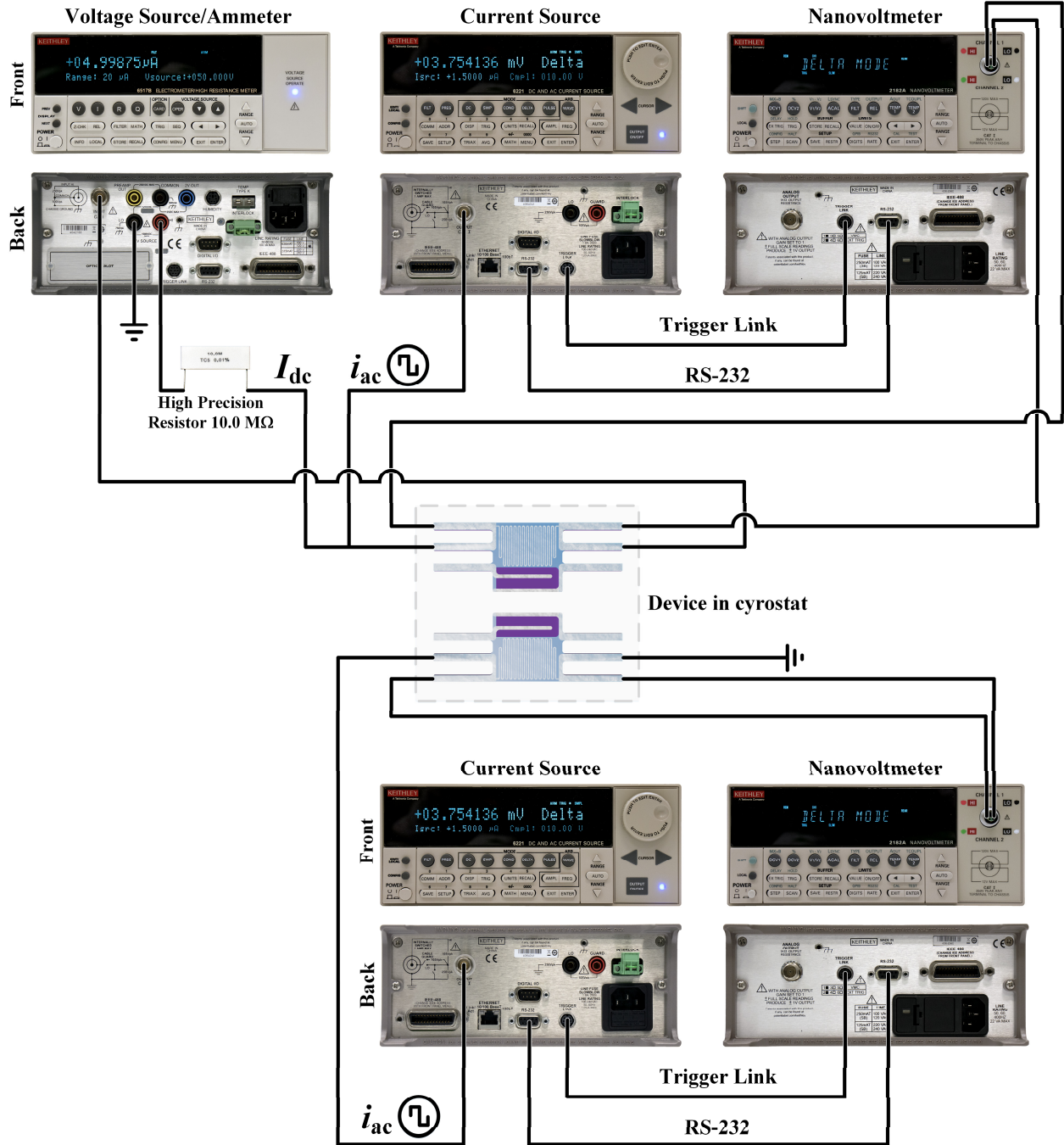
Figure S4. Experimental setup for the DC reversal technique established in this work.

Table S1. *Summary of the optimal settings of the Delta Mode (6221/2182A) for the suspended microthermometry technique using a 6517B voltage source and ultra-precision resistor as a voltage-to-current converter. "h" denotes heating PRT, "s" denotes sensing PRT.*

User Defined Parameters for Measurement			
Delta Mode to measure R_h and R_s			
Keithley 2182A		Keithley 6221	
R_h Sensivity (mV)	100	$i_{ac,h}$ (μA)	1.5
R_s Sensivity (mV)	10	$i_{ac,s}$ (μA)	1.5
Num Point/Line Cycle h	1	AC Current Delay h (s)	0.15
Num Point/Line Cycle s	1	AC Current Delay s (s)	0.002
Analog Filter h	ON	Output low h	Earth Ground
Analog Filter s	ON	Output low s	Earth Ground
Digital Filter h	OFF	Triax Inner Shield h	Cable Guard
Digital Filter s	OFF	Triax Inner Shield s	Cable Guard
DC heating current source			
Keithley 6517B			
Voltage Output	Enable	Meter Connect	Enable
$V_{dc,min}$ (V)	-300	I_{dc} Sensivity (μA)	200
$V_{dc,max}$ (V)	300	$R_{dc,heating}$ (MΩ)	10
Typical noise (ppm) of delta mode at 375K (f_h = 2.97 Hz, f_s = 22.37 Hz)		Typical noise (ppm) of delta mode at 4K (f_h = 2.97 Hz, f_s = 22.37 Hz)	

Table S2. *Summary of temperature and thermal conductance resolution for the DC reversal and lock-in techniques. The measured total (pooled) standard deviation of the sensing temperature rise, σ_{temp}, and the measured standard deviation of the background thermal conductance σ_{Gbg} compare favorably with the NET_s and NEG values.*

DC Reversal Technique						
T_o [K]	$NET_{Johnson}$ [mK]	$NET_{temperature\ drift}$ [mK]	NET_s [mK] a)	σ_{temp} [mK]	NEG [pW/K] b)	σ_{Gbg} [pW/K]
375	1.24	1.99	2.35	2.62	22.75	26.42
350	1.91	1.10	2.21	2.25	22.30	12.62
300	0.96	0.94	1.35	1.47	12.63	8.43
290	0.93	1.08	1.38	1.60	12.72	13.54
250	0.81	0.69	1.07	1.30	9.50	6.60
200	0.67	0.80	1.04	1.29	8.61	6.40
150	0.53	0.77	0.93	1.00	7.23	3.71
100	0.37	0.63	0.73	0.83	4.85	3.46
75	0.31	0.49	0.58	0.96	3.42	6.16
50	0.24	0.26	0.35	1.03	1.66	2.63
40	0.22	0.19	0.30	1.14	1.24	3.49
30	0.21	0.29	0.36	1.12	1.21	1.73

Lock-in Technique							
T_o [K]	$NET_{Johnson}$ [mK]	$NET_{temperature\ drift}$ [mK]	$NET_{lock\text{-}in}$ [mK]	NET_s [mK] a)	σ_{temp} [mK]	NEG [pW/K] b)	σ_{Gbg} [pW/K]
375	0.43	6.98	6.78	7.15	11.55	68.48	83.32
350	0.40	1.74	6.40	6.65	8.81	64.65	50.53
300	0.35	2.11	5.78	6.16	8.67	55.19	23.30
290	0.34	2.35	5.64	6.12	9.97	54.23	28.56
250	0.29	1.69	5.14	5.42	6.71	45.18	19.50
200	0.24	1.20	4.49	4.65	6.18	35.99	23.68
150	0.19	0.84	3.81	3.91	5.82	27.98	13.76
100	0.14	0.88	3.12	3.24	4.80	19.06	13.12
75	0.11	0.55	2.79	2.84	4.82	14.31	13.07
50	0.09	0.26	2.59	2.60	4.95	10.28	6.08
40	0.08	0.34	2.64	2.67	4.35	9.19	4.57
30	0.07	0.38	2.57	2.60	4.54	9.41	10.59

a) $NET_s^2 = NET_{Johnson}^2 + NET_{temperature\ drift}^2$

b) $NEG = G_b \cdot NET_s / (\Delta T_h - \Delta T_s)_{max}$

Supplementary References

[S1] A. Daire, W. Goeke, and M. A. Tupta, Keithley Instruments, Inc. http://www.tek.com/sites/tek.com/files/media/document/resources/Lock-In%20WP.pdf